Front. Earth Sci. 2018, 12(2): 381–396
https://doi.org/10.1007/s11707-017-0651-2

RESEARCH ARTICLE

Analysis of three echo-trainings of a rainstorm in the South China warm region

Zhiying DING (✉)[1,2], Lei QIAN[1,2,3], Xiangjun ZHAO[1,2], Fan XIA[1,2]

1 Key Laboratory of Meteorological Disaster, Nanjing University of Information Science and Technology, Nanjing 210044, China
2 College of Atmospheric Sciences, Nanjing University of Information Science and Technology, Nanjing 210044, China
3 Anhui Meteorological Observatory, Hefei 230061, China

Abstract A rainstorm which occurred between May 22 and 23, 2014 in Guangdong Province of the South China warm region was simulated by using the ARW-WRF model. Three "echo-trainings" over the rainstorm center were analyzed and the results of both the simulation and observational analysis showed that this rainstorm process was composed of three stages. In the first stage, gravity waves triggered the simultaneous but relatively independent formation of linear convection and convective cells, which moved toward the northeast through the rain center, thus creating the echo-training. In the second stage, with the formation of cold outflow, new convective cells were continuously created in the southwest and northwest of the rain area and then gradually moved to merge into the northeast rain area, thus forming a new echo-training. In the third stage, multiple rain bands above the rain area moved southeastward and passed through the strongest precipitation center, thus creating the third echo-training. The model simulation showed that a substantial warming appeared at 900 hPa before the convective initiation, leading to the formation of a stable layer below 900 hPa, which was the primary cause for the gravity waves that triggered the multiple convective cells. The multiple convective cells formed the convective line, following which new convection was formed from the cold outflow in its southwest and northwest directions. The new convection in the southwest maintained the rain band; however, the new convection in the northwest, combined with the rain band of the north, formed a large radar reflectivity area and consequently, a larger MCS.

Keywords convective line, gravity wave, echo-training, back building

Received May 25, 2016; accepted March 12, 2017

E-mail: dingzhiying@nuist.edu.cn

1 Introduction

The South China region is frequently under the influences of low-latitude systems (such as easterly waves and the northern South China Sea monsoon trough) during the pre-summer rainy season. The rainstorms are often dominated by the convergence zone of the southwesterly and southeasterly monsoonal flows and the monsoon surges. Moreover, the uplift and blocking of complex terrain, heterogeneous heating, and the land–sea temperature difference combine to affect the weather systems, leading to frequent and complex meso- and micro-scale convective systems (Xue, 2000; Zhao and Wang, 2009). Such small scale (e.g., meso-β, meso-γ) systems also interact with each other under favorable large-scale conditions, and eventually organize and develop into larger-scale systems, i.e., Mesoscale Convective Complexes (MCC) and Mesoscale Convective Systems (MCS) (Knupp and Cotton, 1987; Li et al., 2013). The extreme rainstorms over the warm South China region usually initialize, develop, and are maintained under the combined influences of these convective systems of different scales. Thus, the structural analysis of the meso- and micro-scale systems and the study on the physical mechanisms of their genesis and development processes are critical for understanding the genesis mechanisms of extraordinary rainstorms in this region.

Meteorologists noticed at a very early stage in the development of the science that gravity waves affect the formation and development of the meso- to micro-scale convective systems and extreme rainfall events. Li (1978) revealed the structural characteristics of gravity waves and pointed out that the gravity wave is one of the primary mechanisms that trigger extreme rainfall under unstable atmospheric conditions. Nachamkin and Cotton (2000), Nachamkin et al. (2000), Xu et al. (2013), and Sun et al. (2012, 2013) also showed that in addition to triggering

extreme rainfall and convective events, the gravity waves could also cause fluctuations in meteorological elements such as temperature and momentum, as well as the propagation of mesoscale convective cells along the gravity waves. Moreover, Gong et al. (2005) also found that a positive feedback coupling system could form between convection and mesoscale gravity waves during the initial stage of the convective storm and the merging stage of the convective cells. In addition to the apparent impact on triggering new storms, the gravity waves also play a certain role in organizing the convective cells into a linear convective system. Besides the impact of the gravity waves on convection, atmospheric scientists also pay close attention to the formation of gravity waves in numerical simulations. Koch and O'Handley (1997) analyzed a gravity wave event that occurred during STORM-FEST by using an automated gravity wave detection system. They found that the solitary wave of depression formed as an upper-level jet stream approached an inflection axis in the diffluent height field downstream of the Rocky Mountains. Koch et al. (2005) investigated the relationship between gravity waves and turbulence associated with an intense upper-level jet/frontal system. The analysis results showed that inertia–gravity waves were generated within a region of unbalanced frontogenesis in the vicinity of a complex tropopause fold. What's more, smaller-scale gravity wave packets within the mesoscale wave field perturbed the background wind shear and stability, promoting the development of bands of reduced Richardson number conducive to the generation of turbulence. Zülicke and Peters (2006), Kuester et al. (2008), Lane and Moncrieff (2008), and Kawashima (2016) found that the deep convection in hurricanes, poleward Rossby wave breaking, multiscale tropical convective systems, and melting-induced cooling also play important roles for the appearance of gravity waves.

Small-scale convective cells or systems have drawn increasing attention in recent years due to increased access to high-resolution radar data and the application of the numerical model. Weisman and Klemp (1984) investigated the effects of directionally varying wind shear on convective storm structure and evolution over a wide range of shear magnitudes by using a three-dimensional numerical cloud model. Nelson and Knight (1987) analyzed the internal structure and growth environment of a hybrid multicellular-supercell storm, whose characteristics were intermediate to classical multicellular and supercell storms, and Nelson (1987) also found that the flow structure of the hybrid multicellular-supercell storm played an important role in hail production. Bauer-Messmer et al. (1998) chosen a squall line and a slow-moving multicellular storm, which developed in close proximity to each other and led to heavy rainfall events, and examined some of the small differences in their storm environment. They found that major differences between the two storms were reflected in the propagation speed and shape of the storms and both differences can be attributed to the degree of internal organization. The research results of Hitchens and Brooks also showed that, in addition to triggering tornadoes, large hail, and damaging winds, supercell thunderstorms were more likely than non-supercells to produce heavy precipitation (Hitchens and Brooks, 2013).

"Echo-trainings" refer to repeated propagation of multiple convective cells over the same location in rain areas causing the occurrence of intermittent heavy rains and further extraordinary rainstorms in local areas (Aylward and Dyer, 2010). Maddox et al. (1979) observed that of the three basic meteorological patterns expected to experience echo-training and storms, it was the common quasi-stationary feature that led to repetitive propagation of storm cells over the same location and to intensive rainfall. Luo et al. (2014) and Wang et al. (2014), in their respective researches on the initiation and organization of extreme-rain-producing mesoscale convective system (MCS), made a comparison between the two modes of echo-trainings different in the direction of movement of convective cells and rainbands. They compared the northeastward "echo training" of convective cells along individual rainbands and the southeastward "band training" of the rainbands along the quasi-linear MCS, playing dissimilar roles in the formation of rainbands and MCS.

Besides the impact of echo-training on storm progression, meteorologists also analyze the mechanism of initiation and maintenance of echo-trainings. Huang et al. (2010) investigated the existence of echo-trainings in the torrential rain caused by typhoon Bilis in eastern Hunan province. Further, they reported that the well-organized secondary circulation caused by discontinuous micro- and meso-scale jet cores at the mid-level troposphere could be one of the main reasons for the formation and maintenance of echo-trainings. Qi et al. (2012) demonstrated the storm-causing effect of echo-training in eastern Hechi and northern Liuzhou in Guangxi Zhuang Autonomous Region, and stability of surface convergence line to be the primary reason for its formation. Chen et al. (2013), through their analysis of the initiation and propagation mechanism for Beijing extremely heavy rainstorm clusters on 21 July 2012, identified distinct echo-training in the movement of storm cells. They also recognized the significant roles played by terrain forcing and low-level wind convergence in raising warm and moist airflow for maintaining the echo-training for long periods of time. In summary, the activity of organized multi-cell storms, the ground quasi-stationary front, and the mesoscale lines maintained for a long time are the main causes for the formation of echo-trainings. However, the maintenance, development, and distribution of meso- and micro-scale convective cells and their sub-vertical circulation along with terrain forcing contribute to the duration of echo-trainings (Ke et al., 2012; Sun et al., 2015).

However, in the current stage, research on the triggering

and maintenance mechanisms of the echo training rarely touches upon the influence of gravity waves. Sun et al. (2012, 2013), through the inversion of actual radar data, analyzed the evolution processes of several multiple thunderstorm cells over the Beijing area, and they proposed that the developing mechanism of the echo-training may have been caused by the triggering and propagation by inertia gravity waves. However, it is still unclear whether gravity waves can play the role of a triggering mechanism of the echo-training or act to modify their evolution. At present, no domestic scholar has employed the numerical model to verify the relationship between gravity waves and the echo-training. In this study, an intense rainstorm in the warm South China region was investigated through diagnostic analysis and numerical modeling, mainly focusing on three aspects: (i) the development and evolution processes of various forms of echo-training in the rainstorm process; (ii) the influence of gravity waves on the triggering and/or evolution of echo-training; and (iii) the changes in organizational structures during convective initiation and development.

2 Weather processes and information

2.1 Data

The data used in this study included the 1°×1° reanalysis data obtained from the National Center for Environmental Prediction (NCEP) at a 6 h interval, and surface hourly rainfall and other meteorological elements from conventional and automated stations, as well as the sounding data collected by the Qingyuan Sounding Station in Guangdong Province (6 h in interval). Furthermore, radar data (6 min interval and 4 km horizontal resolution) at the Guangzhou and Yangjiang stations from 12:00 on May 22 to 06:00 on May 23, 2014 (UTC), were used. The black "X" marks and the black triangle in Fig. 1(a) represent the locations of the two radar stations in Guangzhou and Yangjiang and the Qingyuan Sounding Station, respectively.

2.2 Analysis of observed precipitation

In May, 2014, long-lasting, large-scale heavy rainfall occurred over South China. In particular, central Guangdong Province was hit by intensive rainfall on May 22 and 23 under the impact of the southern branch trough and a low-level jet stream. Figure 1 shows the 22 h observed rainfall distribution from 18:00, May 22 to 16:00, May 23 (UTC), exhibiting a northwest–southeast orientation with the maxima located close to 23.6°N, 113.9°E and reaching 420 mm. The synoptic analysis of this period indicated that there was an east–west near-surface frontline in northern Guangdong Province at around 900 hPa at 23:00 and that the precipitation area was under the control of the warm air at the south side of the frontline (Fig. 2(a)). The analysis also revealed a 500 hPa trough-ridge-trough pattern over the Eurasian continent at mid to high latitudes. The southern branch trough over the low latitudes was located over central Guangxi Zhuang Autonomous Region, and

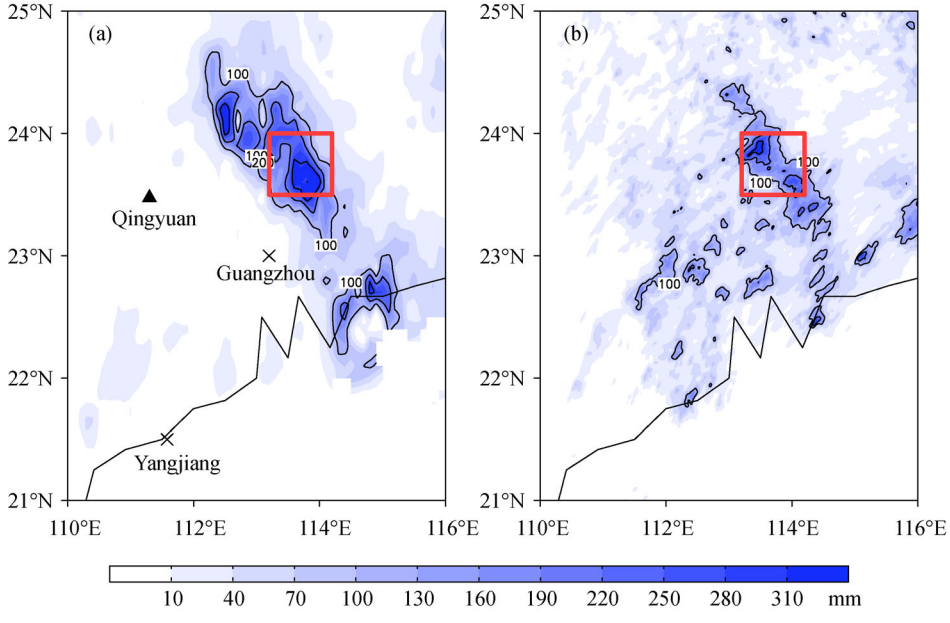

Fig. 1 The distribution of 22-h accumulated surface precipitation from 18:00 on May 22 to 16:00 on May 23, 2014 (UTC) (color shades; unit: mm) derived from (a) the surface hourly rainfall data from conventional and automated stations and (b) the model simulation from the finest-resolution (1.5 km) domain. The black "X" marks represent the locations of the two radar stations in Guangzhou and Yangjiang. The black triangle represents the location of the Qingyuan Sounding Station. The red frames represent strong precipitation center areas in Fig. 5(a).

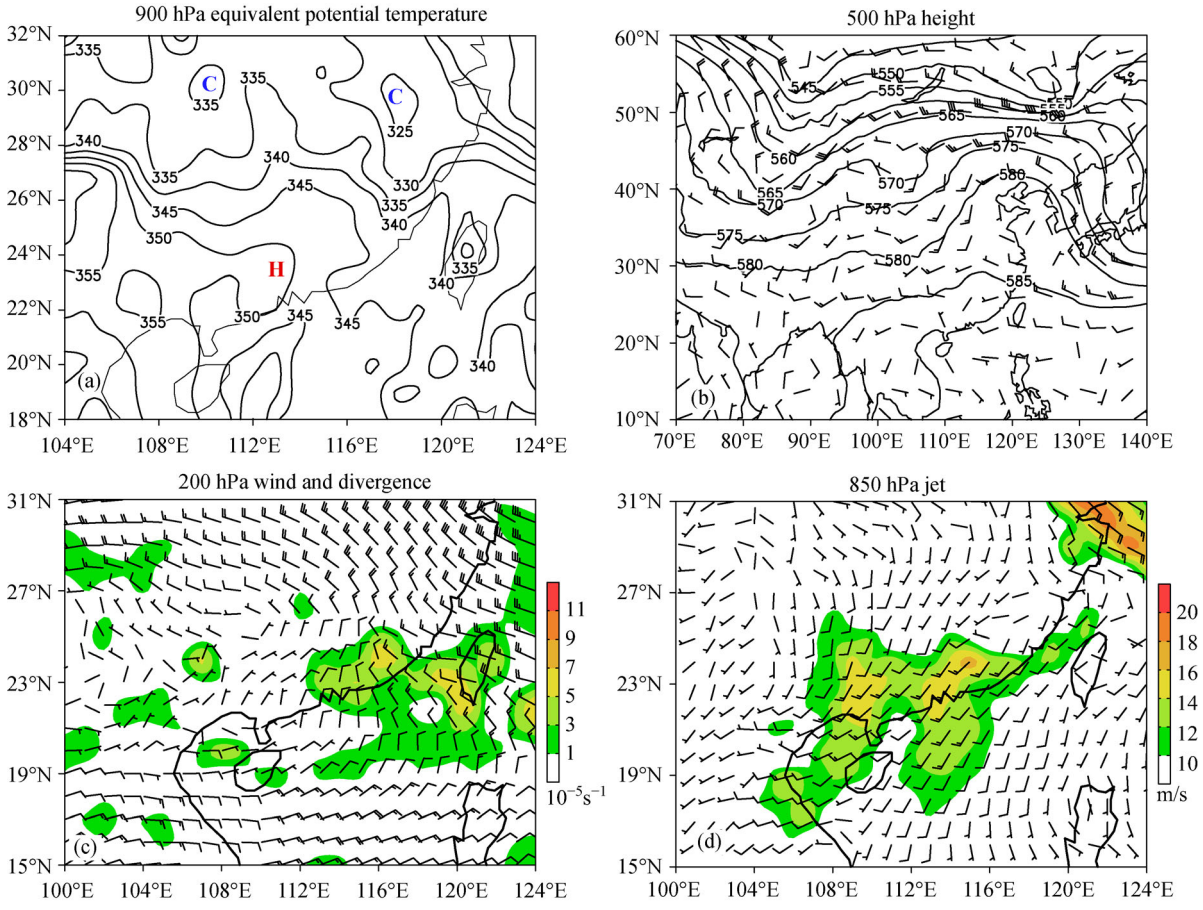

Fig. 2 (a) 900 hPa equivalent potential temperature (contour lines; unit: K), (b) 500 hPa height field (solid lines; unit: dagpm) and wind field (wind barbs; unit: $m \cdot s^{-1}$), (c) 200 hPa wind field (wind barbs; unit: $m \cdot s^{-1}$) and divergence field (color shades; unit: $10^{-5}s^{-1}$), (d) 850 hPa low-level jet stream (wind barbs; unit: $m \cdot s^{-1}$) and wind magnitude (color shades; unit: $m \cdot s^{-1}$) at 00:00 on May 23 (UTC). Capital letters C and H represent 900 hPa cold and warm areas, respectively.

the rain area was located ahead of the trough (Fig. 2(b)). The rain areas were under the influence of divergent air flow on the northeast side of the South Asia high pressure system at 200 hPa (Fig. 2(c)) and southwest–northeast low-level jet stream at 850 hPa (Fig. 2(d)), respectively. This configuration was not only conducive to convective initiation and development, but also provided a channel of water vapor to supply the extraordinary rainstorm (The figure is not shown). In summary, the primary synoptic-scale factors that affected this intense rainstorm were the 200 hPa South Asia high, the 500 hPa southern branch trough, and the 850 hPa low-level jet stream.

2.3 Analysis of observed radar reflectivity

Figures 3(a)–3(f) show the observed horizontal distribution of radar reflectivity at about 3 km above the ground level in the rainfall area from 16:00 to 23:00 on May 22 (UTC). Figure 3(a) exhibits several scattered convective cells appearing in the rainfall area at 16:00, all of which show a relatively weak intensity. The cells gradually developed and at 16:30 the relatively intensive cells (reflectivity > 40 dBZ) lined up over the north, central, and south parts of the rain area, all along the southwest–northeast orientation (Fig. 3(b)). By 17:30, three linear convective structures of southwest–northeast orientation were formed (Fig. 3(c)). In the meantime, there were new convective cells taking shape on the northwest and southwest side of these convective lines. Those new convective cells on the southwest side continuously moved northeastward to maintain the convective line; however, those on the northwest side moved northwestward and weakened in the opposite direction to the system and on the rear flank of the system, and finally evolved into stratiform clouds (Figs. 3(d) and 3(e)). After 20:00, the three convective lines and the accompanying stratiform clouds merged gradually (Fig. 3(f)) to form a northwest–southeast MCS. Overall, this rainstorm was caused by multiple northeast–southwest convective lines that were continuously developing on the northwest side and eventually merged into an MCS. Therefore, the key questions to answer here are the mechanisms of triggering and formation of the convective

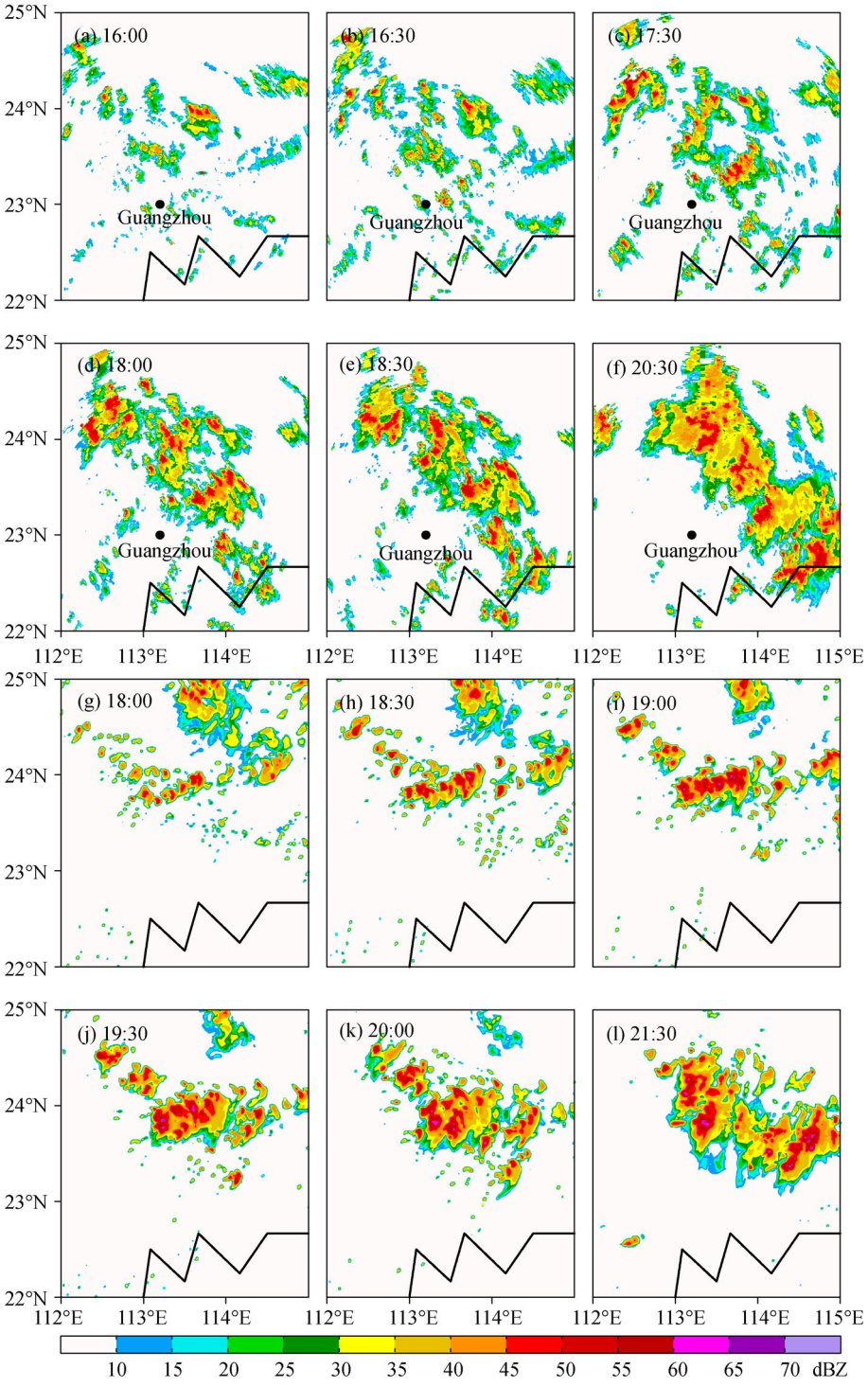

Fig. 3 (a)–(f) observed, (g)–(l) simulated radar reflectivity (color shades, unit: dBZ) on May 22, 2014 (UTC). (a)–(f) represent 16:00, 16:30, 17:30, 18:00, 18:30, and 20:30, and (g)–(l) represent 18:00, 18:30, 19:00, 19:30, 20:00, and 21:30, respectively (Because the convective lines in the simulations appeared 2 h later than they did in the observations, so the time of the simulated figures was delayed 1–2 h compared with the observed figures to show the best match possible in observed and simulated results). The black dot marks represent the locations of the radar station in Guangzhou.

lines, and the mechanisms of proliferation of the southwest and northwest oriented convective cells. However, it is insufficient to rely on the radar and reanalysis data to answer these key questions. To obtain more detailed data of this rainstorm, high-resolution numerical model simulations were performed.

3 Numerical simulation and results analysis

3.1 Simulation scheme

In this study, the mesoscale model WRFV3.2.1 (Skamarock et al., 2008; co-developed by NCEP, NCAR, and other American scientific institutions) was used to simulate the rainstorm that occurred in the central Guangdong Province from 12:00 on May 22 to 18:00 on May 23, 2014 (UTC). The initial and boundary conditions of the model were provided by the 6-hourly NCEP 1°×1° reanalysis data. Three nested model domains (as shown in Fig. 4) centered at 24°N and 113.5°E were configured with 226×145, 328×271, and 478×481 horizontal grid points and (13.5, 4.5, and 1.5) km horizontal resolutions for each domain, respectively (40 layers in total in the vertical direction). The model was integrated for a total of 30 h from 12:00 on May 22 to 18:00 on May 23, 2014 (UTC), producing output every 10 min for the innermost domain. The Lin microphysical parameterization scheme was adopted for all domains. Yin et al. (2014) analyzed the statistical results of sensitivity experiments against the cloud microphysics parameterization schemes of the mesoscale numerical model in China. They found that the Lin scheme in the WRF model performed well in simulations. The Kain–Fritsch cumulus parameterization scheme was used for the 13.5-km grid domain. Other parameterization schemes adopted for modeling purposes are listed in Table 1.

3.2 Comparisons of rainfall distribution

Comparison of Fig. 1(a) and Fig. 1(b) shows that the simulated rainfall distribution was similar to that of the observed one, both having a northwest–southeast rain band and a simulated 22 h central accumulated rainfall of 330 mm. The probability density functions of 22 h accumulated surface precipitation in rainfall area (110°E–116°E, 21°N–25°N) also show consistent distribution characteristics for the observed and simulated results, with the high value of probability concentrates in the zone of 0–50 mm (Fig. 5(b)). However, the simulated rainfall area was narrower than the observed rainfall area and also located slightly to the southeast of the observed area. Figure 5(a) indicates that the amount of hourly rainfall averaged over the central rain area (113.2°E–114.2°E, 23.5°N–24°N) shows consistent change characteristics for observed and simulated rainfall, both with unimodal distributions, and there is only a 1 h lag between the two peaks. However, comparison to the real case indicated that the simulated rainfall declined sharply after 04:00, May 23 (UTC), leading to much lower total rainfall at the rain center than that of the observed rainfall. The primary reason for this was the shift of model rain band toward the southwest after 04:00. Overall, the simulated rainfall area, intensity, and trend were basically consistent with the observations.

3.3 Comparison of radar echo distribution

Both the observed (Figs. 3(a)–3(f)) and simulated (Figs. 3(g)–3(l)) radar echoes present similar evolutions. Figure 3(g) shows a primary northeast–southwest convective line at 18:00 on May 22 (UTC) in the rainstorm area, with an intensity greater than 50 dBZ. A few new convective cells were scattered on the northwest side of the convective line. At 18:30, the entire convective line showed a tendency of development toward the northwest (Fig. 3(h)). The model was not able to simulate the three larger scale convective lines in the rainstorm area during the early stages and the primary convective line appeared 2 h later than it did in the observations. However, the primary convective line showed a northwestward development tendency following its formation, which was consistent with the observed evolution. By 19:30 (Fig. 3(j)), another convective line appeared to the south of the

Table 1 Parameterization schemes for the simulation

WRFV3.2.1	D01	D02	D03
Horizontal resolution/km	13.5	4.5	1.5
Horizontal grid points	226×145	328×271	478×481
Microphysical process scheme	Lin	Lin	Lin
Long-wave radiation scheme	RRTM	RRTM	RRTM
Shortwave radiation scheme	Dudhia	Dudhia	Dudhia
Cumulus convection scheme	K-F	——	——
Surface-layer physics scheme	Monin-Obukhov	Monin-Obukhov	Monin-Obukhov
Planetary boundary layer scheme	YSU	YSU	YSU
Land surface physics scheme	Noah	Noah	Noah

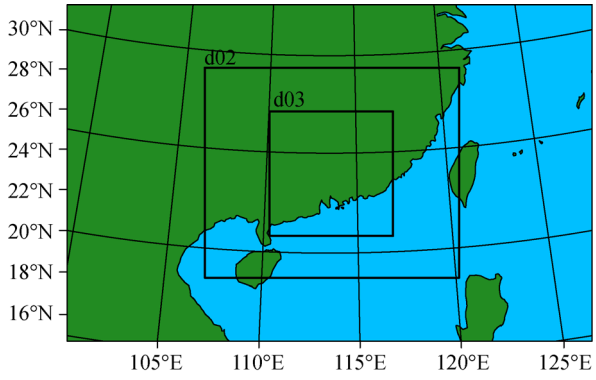

Fig. 4 Sketch map of the triple nested grids.

primary convective line, with convective developments also seen to the north of the primary convective line that did not develop into a secondary convective line. Immediately beside the northern part of the primary convective line, the emerging convective line corresponded to the proliferation found in the observations (Figs. 3(d) and 3(e)). Multiple convective lines developed afterwards (Fig. 3(k)) and merged into a larger-scale MCS by 21:30 (Fig. 3(l)). Although the convective lines on the south and north sides of the primary convective line appeared late in the simulations, overall, the simulated locations and evolution of the convective lines were in good agreement with the observations and could be used in meso- and micro-scale structural analysis.

4 Echo-training during the rainstorm

Based on the above-mentioned analysis of observed and simulated results, the radar echo of this rainstorm area was combined with several northeast–southwest banded structures. Further analysis of the observed results indicated that these line echoes were created by several relatively weak convective cells and that the formation of these convective cells constituted the primary factor that initiated this rainstorm. On the observed radar echo chart at the height of 3 km from 17:00 to 20:00 (UTC), there were a total of six maximum-value centers (the radar echo maximum-value areas marked as A–F in Figs. 6(a)–6(d) represent rain clusters), and these rain clusters moved northeastward and passed through the maximum rainfall center in succession. Moreover, in Fig. 6(c), the rain clusters A, B, and C clearly present a northward proliferation (more clearly manifested in Figs. 3(d) and 3(e)), which passed through the maximum rainfall center. This type of proliferation is also the major cause of the formation of larger-scale MCS through the continuous widening of multiple rain bands and the shortening of distances between rain bands. After the passage of the first round of rain clusters (around 20:00, Fig. 6(d)), the front end of the rain band was weakened. However, new rain clusters appeared on the southwest side of the previous rain clusters (rain clusters labeled as G–J in Figs. 6(d)–6(f)). These rain clusters continued to move northeastward and formed a new series of rain clusters, which lasted until 03:00 on May 23. Subsequently, the northeastward motion of the rain clusters became indiscernible. The appearance of the southwest cloud clusters also became less frequent, presenting a clearer northwest–southeast movement of the rain bands, and the rainfall gradually tapered off.

The above-mentioned analysis indicated the occurrence of a total of three stages of echo-training during this rainstorm. The first was the convective line stage when multiple rain clusters appeared in a northeast–southwest linear orientation, moved northeastward, and passed

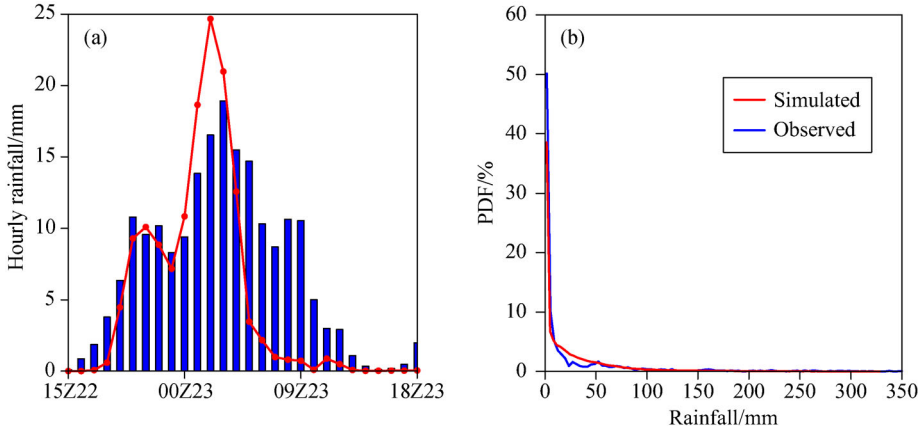

Fig. 5 (a) Change of the regional average precipitation of the strong precipitation center (113.2°E–114.2°E, 23.5°N–24°N) from 15:00 on May 22 to 18:00 on May 23 (UTC) (unit: mm) (the straight square columns represent the observed results, and the red line represents the simulated results). (b) The probability density functions of 22-h accumulated surface precipitation in rainfall area (110°E–116°E, 21°N–25°N) from 18:00 on May 22 to 16:00 on May 23, 2014 (UTC). The blue and red solid lines represent the observed and simulated results, respectively.

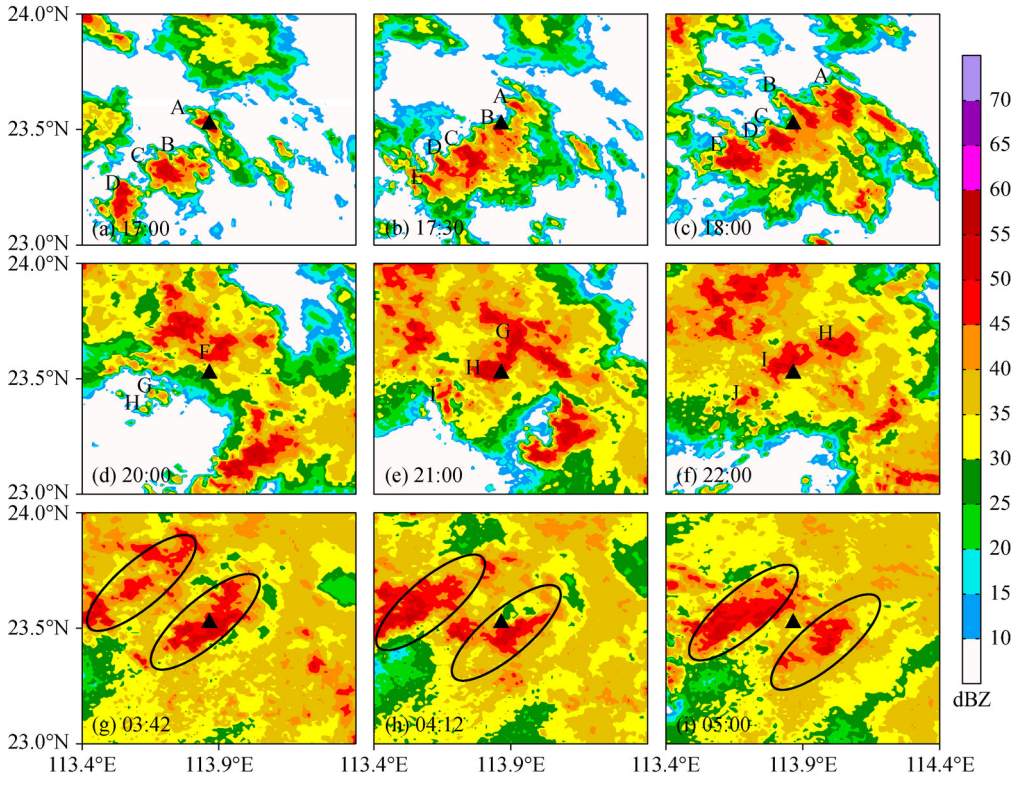

Fig. 6 Observed radar reflectivity at the height of 3 km (color shades; unit: dBZ) between May 22 and May 23 (UTC). ((a)–(i) respectively, represent 17:00, 17:30, 18:00, 20:00, 21:00, 22:00, 03:42, 04:12, and 05:00. The black triangle represents the location of the observed maximum precipitation center, and letters A–J, respectively, represent the rain clusters passing the maximum precipitation center and its nearby area).

through the maximum rainfall center. The second was the continuous genesis stage when new rain clusters were continuously formed at the southwest side of the rainfall center and moved toward the rainfall center. The third stage was dominated by the movement of the entire rain bands toward the southeast. In the late stage of the strong precipitation, the development of the convective rain clusters at the southwest side of the rain band became less intensive, the entire rain band moved toward the southeast, and passed through the rainfall center.

Simulation-based analysis also yielded similar results; however, the rain clusters started late and ended early on the whole (the simulated radar reflectivity on 700 hPa was adopted because the height of 700 hPa is close to the height of 3 km). The first stage took place between 18:00 and 19:50 (Figs. 7(a)–7(d)), and the second stage occurred between 20:00 and 23:00 (Figs. 7(d)–7(f)), followed by the third stage (Figs. 7(g)–7(i)). A further comparison of the observed and simulated results of the differences between various stages of the echo-training indicated that the new cells continuously emerged at the southwest side of the observed precipitation center and moved eastward between 18:00 on May 22 and 03:00 on May 23, and that the motion of the backbuilding new cells in the simulated results was limited to between 18:00 on May 22 and 00:00 on May 23. As a result, the duration of the second stage of the echo-training near the actual maximum precipitation center was longer than that obtained from the simulated results, which caused the cumulative precipitation of the simulated precipitation center to be less than that of the observed results.

5 Analysis of the formation and triggering mechanism of the convective line in the first stage of the echo-training

5.1 Formation of the convective line

The above-mentioned analysis indicated that this rainstorm experienced three stages of echo-training, of which the first was mainly caused by the northeast–southwest convective line composed of multiple convective cells and which moved in the northeast direction. The cause of the formation of these convective cells constituted the primary problem discussed below. Starting from 17:10 on May 22 (UTC), (Figs. 8(a) and 8(b)), several meso-γ scale convective cells appeared in the rainstorm region with radar echoes exceeding 35 dBZ. These convective cells continued to develop and intensify while moving toward

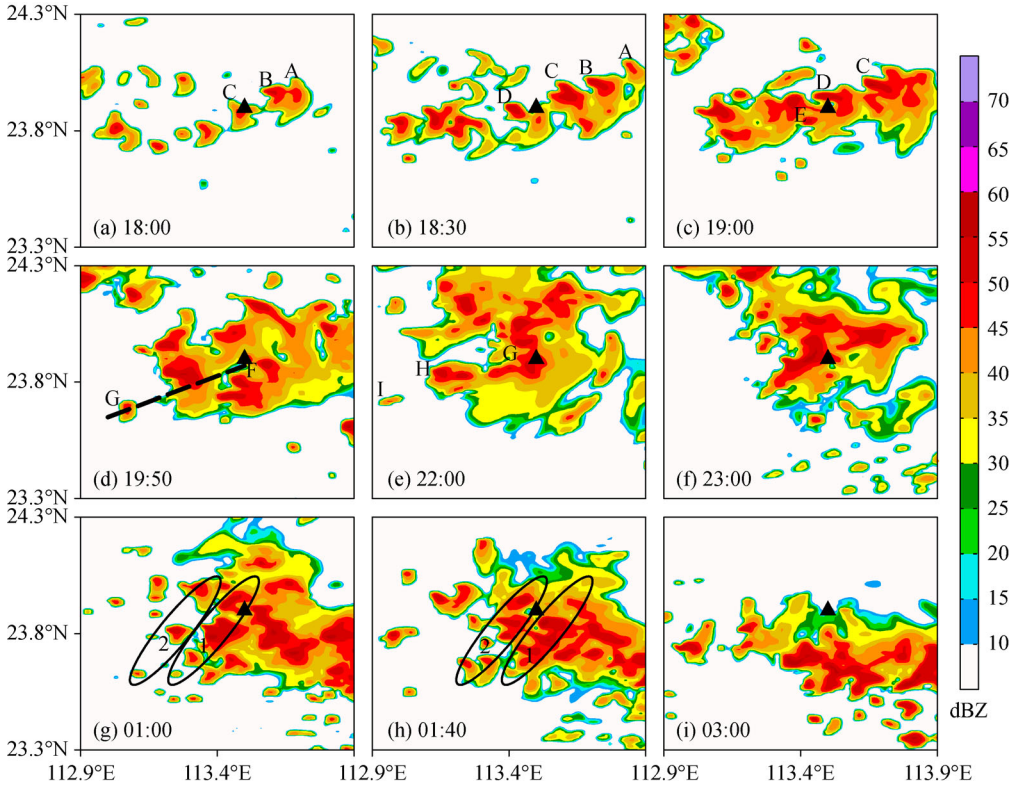

Fig. 7 Simulated radar reflectivity on 700 hPa (color shades; unit: dBZ) between May 22 and May 23 (UTC) ((a)–(i), respectively, represent 18:00, 18:30, 19:00, 19:50, 22:00, 23:00, 01:00, 01:40, and 03:00. The black triangle represents the location of the simulated maximum precipitation center and letters A–I, respectively, represent the rain clusters passing the maximum precipitation center and its nearby area. The numbers 1 and 2 represent rain bands and the black dashed line represents the location of the inclined section shown in Fig. (13).

the northeast. Up until 18:00, they aligned along a northeast–southwest direction and formed the primary convective line (Fig. 8(c)). As several new convective cells formed in the southwest and merged into the primary convective line, a few new convective cells also formed on the northwest side of the primary convective line. By 18:20, a new convective line had formed on that side (Fig. 8(e)). During the formation process and when most of the convective cells had developed into a certain stage (having exceeded 40 dBZ), the 500 hPa equivalent potential temperature exhibited closed local warm bubbles near the convective cells, which moved toward the northeast as the convective cells continued to develop and intensify.

The inclined vertical section of simulated equivalent potential temperature and radar reflectivity was prepared along the primary convective line (black dashed line, northeast–southwest direction, as shown in Fig. 8). Starting at 16:10, a relatively weak updraft at low level began to emerge below 800 hPa in the convective area. Then, at 16:20, the low-level warm moist vapor was transported upward along with the weak updraft, which began to release the latent heat of condensation. As a result, the low-level isosurface of equivalent potential temperature bulged upward (illustration omitted) and presented clearly discernable disturbances (Fig. 9(a)). Accompanied by the continuous intensification of warm moisture updrafts at the low level of the convective line and their northeast extension, the low-level isosurface of equivalent potential temperature also bulged upward and formed warm air columns, which then moved eastward. After 17:50 (Fig. 9(b)), new convective cells and warm air columns were successively formed at the southwest side of the warm air columns, which resulted in the northeast–southwest linear distribution of multiple convective cells along this inclined section. This analysis motivated us to search for a solution to the following issues: the factors that caused the weak updrafts prior to the formation of multiple convective cells; and any triggering mechanisms that enhanced the updraft, caused the bulge in the isosurface of equivalent potential temperature, and formed the warm air columns. Therefore, in the following sections, an attempt was made to explain the above-mentioned issues.

5.2 Characteristics and emergence conditions of the gravity waves

The 25-point low-pass filtering method proposed by Xia

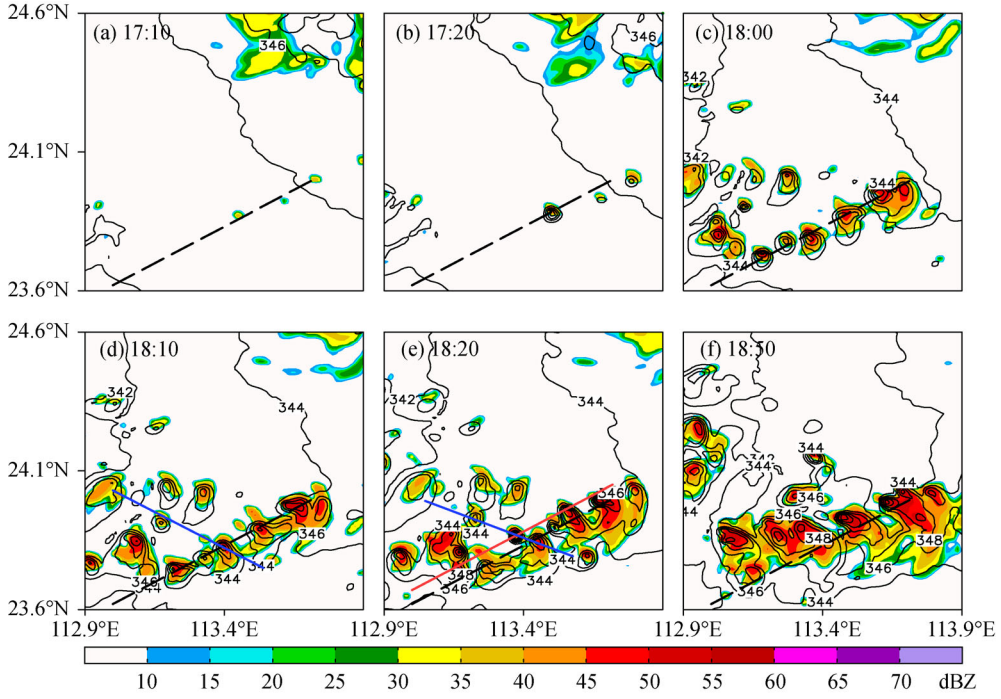

Fig. 8 Simulated equivalent potential temperature on 500 hPa (contour lines; unit: K) and radar reflectivity on 700 hPa (color shades; unit: dBZ). The black dashed line represents the location of the inclined section shown in Fig. 9, the blue solid line represents the location of the inclined section shown in Fig. 13, and the red solid line represents the location of the new convective line. (a), (b), (c), (d), (e), and (f) represent 17:10, 17:20, 18:00, 18:10, 18:20, and 18:50 (UTC), respectively.

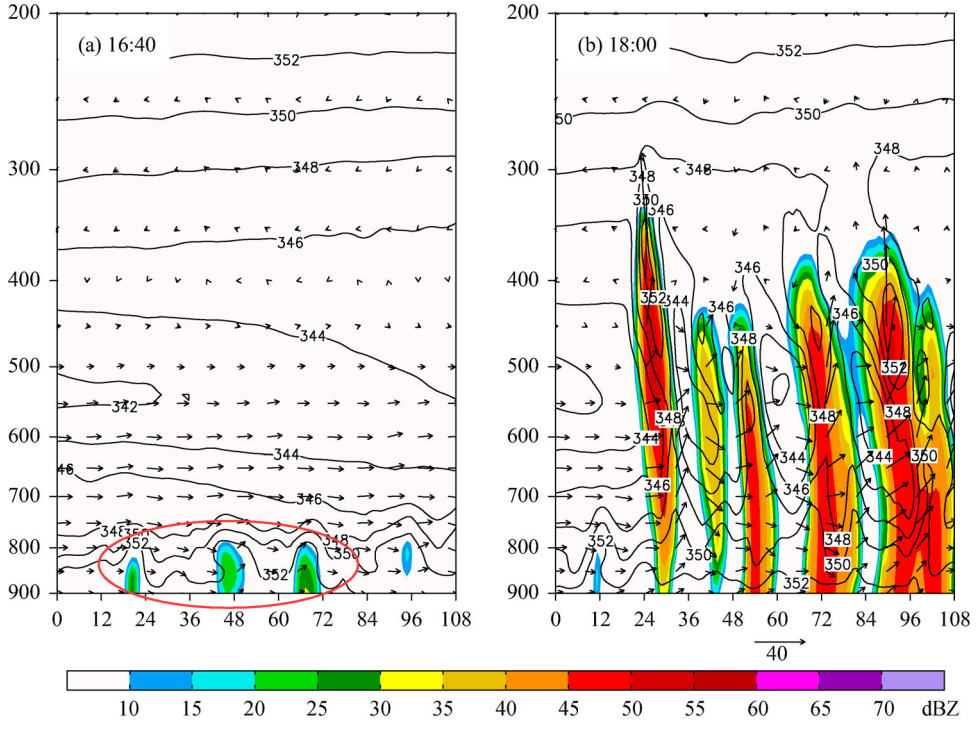

Fig. 9 Inclined vertical section of simulated equivalent potential temperature (contour lines; unit: K), radar reflectivity (color shades; unit: dBZ), and vertical circulation (arrows, vertical velocity was magnified by 10 times; unit: $m \cdot s^{-1}$) along the black dashed line shown in Fig. 8. (a) and (b) represent 16:40 and 18:00 (UTC), respectively.

et al. (1983) was adopted to separate small and medium-scale weather information from the large-scale environment field. Further, the filtered whole-layer divergence, vorticity, vertical velocity, and disturbance potential temperature were compared in terms of their distributions along the primary convective line (i.e., along the black dashed line shown in Fig. 8). The results indicated that, at the height of 900 hPa, both vorticity and divergence of the convective line manifested a discernable pattern of alternative distribution of positive and negative centers from 16:10 on May 22 (UTC) and that divergence was $\pi/2$ phases behind the vorticity. The distribution comparison between vertical velocity and disturbance potential temperature at the same moment showed that both of them clearly presented an out-of-phase distribution pattern, indicating that the train of waves emerging at the low level of the convective line before the genesis of convective cells was one of the gravity waves. Further analysis indicated that, although the gravity wave emerged at the height of 900 hPa in the convective area as early as 16:10, they were limited to the southwest side of the 21st point in Fig. 10 (Figs. 10(a) and 10(b)). Then, with the continuous extension in the northeast direction, the gravity wave completely covered the convective area at 16:50 (Figs. 10(c) and 10(d)). As indicated by the phase changes of the peaks and valleys of the gravity wave from one moment to another, the wave manifested a characteristic of propagation toward the northeast direction with time. To further analyze the movement characteristic of the gravity wave, the difference in the divergence at 900 hPa between the two moments was calculated as the divergence increment, which was used to manifest the change and movement of the wave with time. The results indicated that, between 16:30 and 16:50, under the influence of the gravity wave, the divergence increments of various points exhibited distinct waves (illustration omitted). The wave

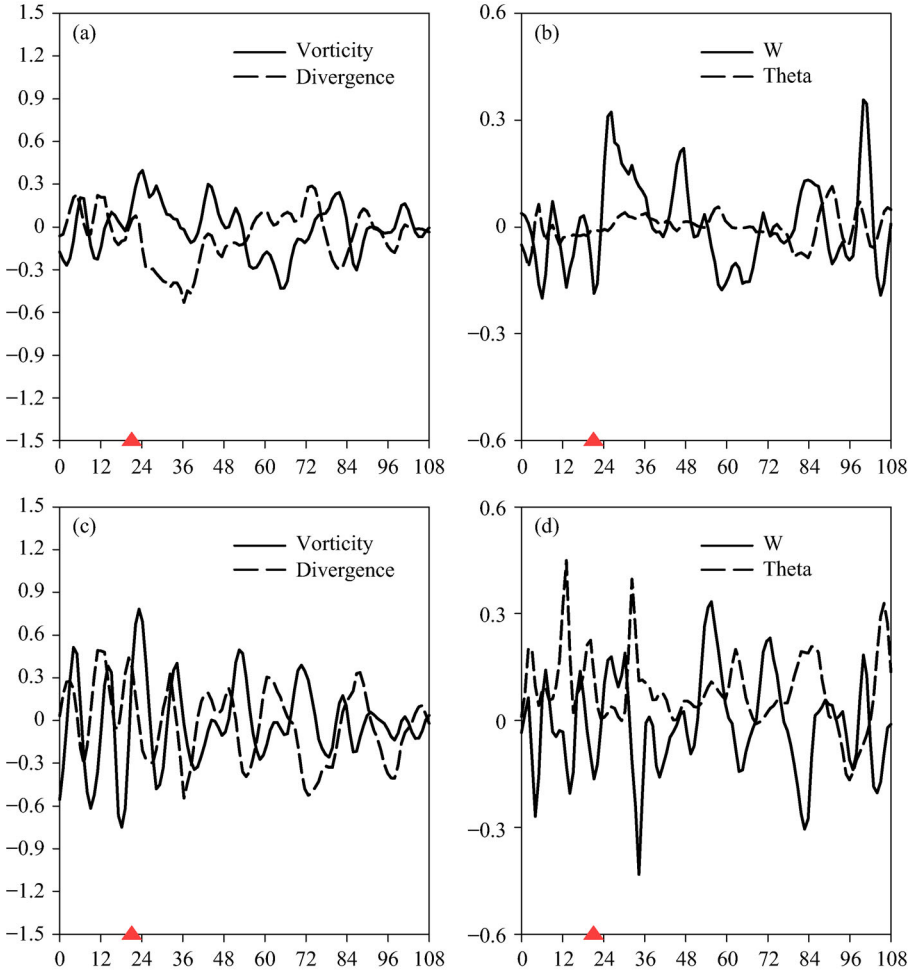

Fig. 10 (a) and (c) simulated vertical vorticity (solid lines; unit: 10^{-3} s^{-1}) and divergence on 900 hPa (dashed lines; unit: 10^{-3} s^{-1}), (b) and (d) vertical velocity (solid lines; unit: $m \cdot s^{-1}$) and disturbance potential temperature on 900 hPa (dashed lines; unit: K) along the black dashed line shown in Fig. 8. (a) and (b) represent 16:10 on May 22 (UTC), (c) and (d) represent 16:50 on May 22 (UTC). The red triangle represents the location of the 21st point.

manifested a characteristic of propagation toward the northeast direction with time, and the propagation velocity was roughly 7–11 grid points/10 min (i.e., 9–15 $m \cdot s^{-1}$), which met the propagation velocity standard of the gravity waves (Li, 1978).

After preparing the inclined vertical section of simulated equivalent potential temperature and relative humidity along the primary convective line, the Richardson Number (*Ri*) at the height of 900 hPa was calculated, followed by the analysis of the environmental conditions favorable for the emergence of the gravity wave. Given that gravity waves mostly take shape in stable layers of $Ri < 0.5$, we adopted $0 < Ri < 0.5$ as the criterion of the emergence of the gravity waves. The expression of *Ri* is $Ri = -\frac{\Delta\theta}{\overline{\theta}} \frac{\Delta p}{\rho(\Delta V_h)^2}$ (Shou et al., 2003), wherein 850 hPa and 950 hPa are introduced as its high and low levels, respectively; $\Delta\theta$ and Δp represent the potential temperature difference and atmospheric pressure difference, respectively, of the two isobaric surfaces; $\overline{\theta}$ represents the average potential temperature on the two isobaric surfaces; and ΔV_h represents the horizontal wind velocity difference between the two isobaric surfaces. Given that the relative humidity of the convective line below 850 hPa in Figs. 11(a) and 11(b) is uniformly above 98% and that the atmosphere is in a saturated state, we adopted the equivalent potential temperature θ_e in place of the potential temperature θ in the original expression. The inclined vertical section of equivalent potential temperature exhibited an unstable convective stratification at the convective line below 600 hPa before 15:00 on May 22 (UTC), and 900 hPa was under the control of the relatively weak southwest wind (illustration omitted). A comparison with *Ri* at 900 hPa at the same moment indicated that *Ri* values near the convective line were all negative (illustration omitted), which was unfavorable for the emergence of the low-level gravity wave. After 15:00, due to the appreciable enhancement of the southwest wind at 900 hPa near the convective line, the warm moist air at its southwest side was transported to the northeast under the action of the

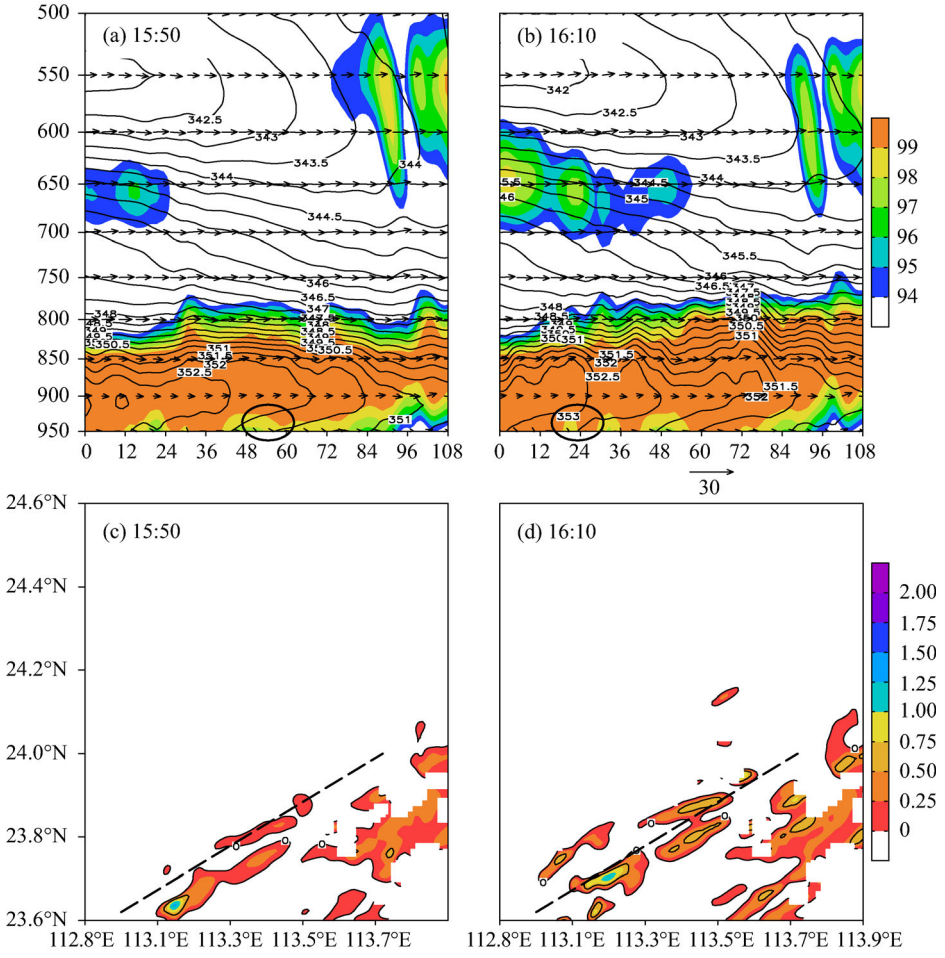

Fig. 11 (a) and (b) Inclined vertical section of equivalent potential temperature (contour lines; unit: K), vertical circulation (arrows; vertical velocity was magnified by 10 times; unit: $m \cdot s^{-1}$) and relative humidity (color shades; unit: %) along the black dashed line shown in Fig. 8. (c) and (d) horizontal distribution of *Ri* on 900 hPa (color shades; contour lines marking the scope of $0 < Ri < 0.5$; the black dashed line represents the location of the primary convective line). (a) and (c) represent 15:50, and (b) and (d) represent 16:10.

wind field, resulting in the formation of appreciable warm advection at the low level of the convective line. A further comparison with the observed sounding curve obtained from the Qingyuan Station at the southwest side of the precipitation center at 18:00 on May 22 showed that the wind direction below 850 hPa clearly exhibited a clockwise rotation with height accompanied by the emergence of a thermal inversion layer (Fig. 12(a)). Under the action of the warm advection, there was an appreciable warming phenomenon of the convective line at 900 hPa, resulting in the formation of a shallow stable layer at the 55th point around 900–950 hPa at 15:50 (Fig. 11(a)). A comparison with the horizontal distribution of *Ri* on 900 hPa at the same moment indicated that the *Ri* at the same location ranged between 0 and 0.25 (Fig. 11(c)), which was favorable for the emergence and development of the gravity wave. After that, along with the continuation of warm advection on 900 hPa, the shallow stable layer at the middle-low level of the convective line continuously extended toward both sides, followed by the formation of a shallow stable layer at the 21st point at 16:10. At the same moment, *Ri* at 900 hPa ranged between 0 and 0.5 (Fig. 11(d)), and the gravity wave emerged. Under the influence of the gravity wave, low-level convergence and updraft of warm moist air occurred in the gravity wave convergence zones, leading to low-level fluctuations of the isosurface of equivalent potential temperature and triggering the release of unstable energy. These phenomena further prompted the genesis of multiple convective cells in the gravity wave convergence zone, which then moved to the northeast direction with fluctuations (Fig. 12(b)).

Thus, the southwest wind transported the warm moist air at the southwest side of the convective line at 900 hPa to the northeast after 15:00, and the resulting warming at 900 hPa further led to the formation of a shallow stable layer at low level of the convective line. This provided a favorable stratification condition and energy source for the emergence of the low-level gravity wave. Under the impact of the gravity wave, the low-level convergence and updraft of the convective line were enhanced and scattered along the convective line, leading to the upward transport of low-level warm moist water vapor and the release of the latent heat of condensation, as well as to the fluctuations of the isosurface of equivalent potential temperature. These phenomena further triggered the release of unstable energy and prompted the genesis of multiple convective cells in the gravity wave convergence zone, which presented a northeast–southwest linear distribution pattern.

6 Convective cell genesis on the rear and northwest flank

Observations and simulation-based analysis discussed above clearly indicated that there was continuous back building of convective cells on the southwest and northwest sides of the northeast–southwest oriented rain band and that it incurred the second stage of the echo-trainings. Discussion on the causes of the two directions of continuous genesis, in particular the difference between the northwest proliferation and the back building, is presented below.

Figures 13(a) and 13(e) showed the cross-section of the newborn convective cell G on the southwest side of the rain band in Fig. 7(d), revealing that cold downdrafts dominated the layers below 500 hPa at 20:00, May 22

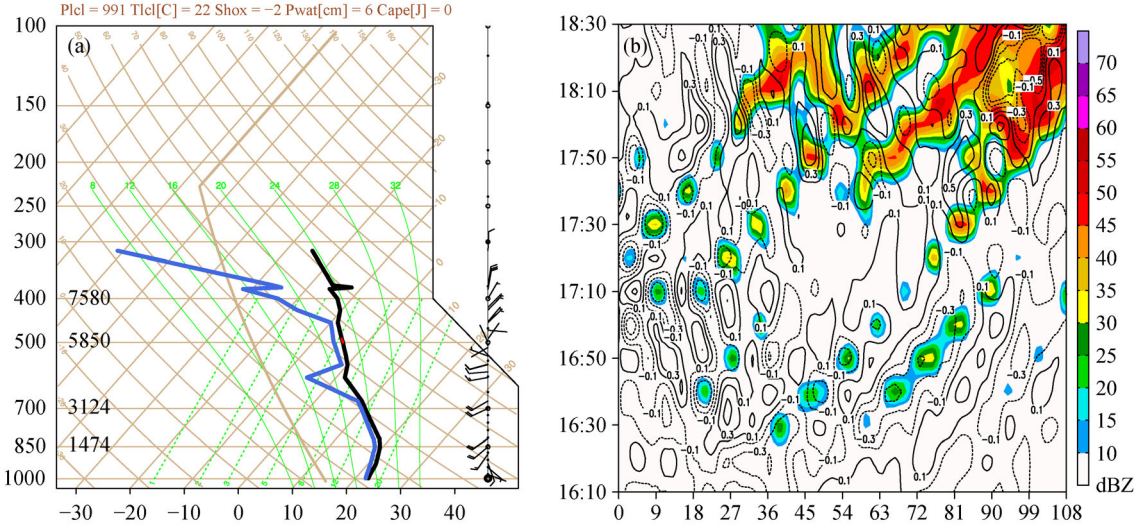

Fig. 12 (a) Vertical profiles plotted on skew T-log P diagram of temperature (the black line) and dew point temperature (blue line) over Qingyuan sounding station at 18:00 on May 22 (UTC). (b) Time-space section of simulated radar reflectivity on 850 hPa (color shades; unit: dBZ) and divergence on 900 hPa (contour lines; unit: 10^{-3} s^{-1}) along the black dashed line shown in Fig. 8 between 16:10 and 18:30 on May 22 (UTC).

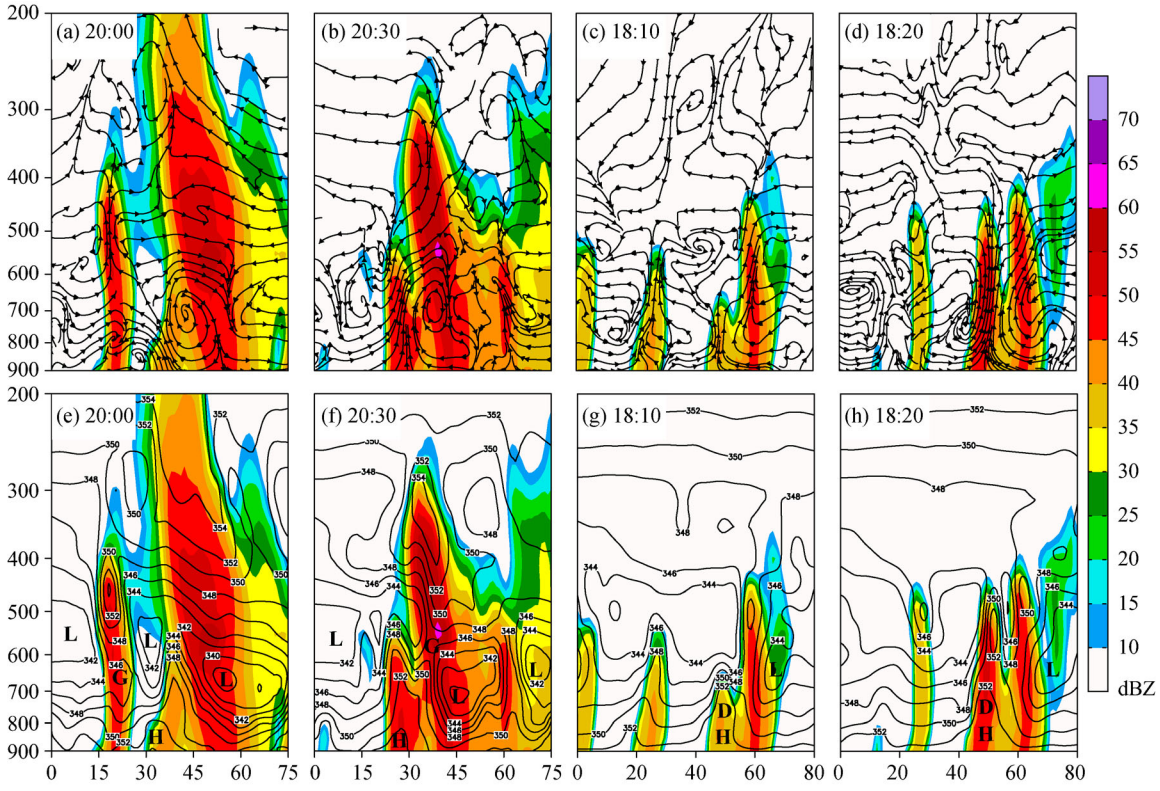

Fig. 13 Simulated radar reflectivity (color shades, unit: dBZ) cross-sections along the black dashed line in Fig. 7(d) for (a) 20:00, (b) 20:30, (e) 20:00, and (f) 20:30 on May 22 (UTC) and along the blue solid line in Fig. 8 for (c) 18:10, (d) 18:20, (g) 18:10, and (h) 18:20 on May 22 (UTC). The divergent wind vertical circulation (stream lines, unit: $m \cdot s^{-1}$) is shown in (a)–(d) and the equivalent potential temperature (contour lines, unit: K) is shown in (e)–(h). Capital letters L and H represent low and high value centers of equivalent potential temperature, respectively. G and D represent the convective cells G and D in Fig. 7.

(UTC) because of raindrop drag and evaporative cooling. When the downdraft reached the 800 hPa layer, it changed to a northeast wind and merged with the southwest warm moist air at the 700 hPa level, causing updraft motion and contributing to the development of the rear flank convective cells (Figs. 13(a) and 13(e)). When the newly generated convective cell matured and merged into the rain band, they produced a new cold downdraft that again merged with southwest warm moist air, which supported the continuous formation of convective cells on the rear flank (Figs. 13(b) and 13(f)) and maintained the convective line.

Figures 7(d) and 7(e) show that the newly generated convective cells on the northwest side contributed to the northwestward extension of the rain band, which merged with another convective line to its northwest, with their rear flank stratiform clouds also combined with the rain band. The vertical cross-section (northwest flank proliferation) perpendicular to the primary convective line (Figs. 8(d) and 8(e)) shows that the development mechanisms of these newly generated convective cells were also triggered by the merging of the cold outflow from the convective line and the low-level warm moist air (Figs. 13(c), 13(d), 13(g), and 13(h)).

In summary, in this case study, the convective cells not only developed on the southwest side to maintain the convective line and the second stage of the echo-trainings, but also on the northwest side, perpendicular to the convective line. The convective cell geneses on both sides were caused by the cold outflow from the convective line. In particular, the development along the direction perpendicular to the convective line enhanced the development of multiple convective lines and their combination into a larger MCS through the shortening of distances between convective lines.

7 Conclusions

This study investigated the warm region rainstorm that occurred between May 22 and May 23, 2014 (UTC) over the central Guangdong Province by numerical simulations by using the ARW-WRF model. The simulations well represented three observed echo-trainings and the development and evolution of the convection.

1) This case included a warm region rainstorm event jointly influenced by the southern branch trough at 500 hPa, the South Asia high at 200 hPa, and the low-level jet

stream at 850 hPa. The rainstorm occurred ahead of the southern branch trough, and the coupling of the convergence area on the left side of the low-level jet and the divergence zone on the northeast side of the South Asia high provided the favorable large-scale environment for the occurrence of the rainstorm.

2) Analysis of the observed and simulated radar echoes around the maximum precipitation center indicated the presence of three stages of echo-trainings during this warm region rainstorm. The first was the convective line stage when multiple rain clusters appeared simultaneously and passed through the maximum precipitation center. The second was the continuous genesis stage when new rain clusters were continuously formed at the southwest side of the precipitation center and moved toward it. The third stage was the stage dominated by multiple entire rain bands moving toward the southeast.

3) The structural analysis of the convective line incurring the first stage of echo-trainings, which occurred both in the observations and model simulations, was conducted. At 900 hPa level, the southwest wind transported the warm moist air at the southwest side of the convective line to the northeast. The resulting warming at 900 hPa of the convection line further led to the formation of a shallow stable layer at low level, which provided a favorable condition and energy source for the emergence of the low-level gravity wave. Under the impact of the gravity wave, the convergence and updraft of the convective line at low level were enhanced and scattered along the convective line, leading to the upward transport of low-level warm moist water vapor and the release of the latent heat of condensation, as well as to the fluctuations of the isosurface of equivalent potential temperature. The induced buoyancy fluctuation triggered the formation of convective cells. Multiple convective cells developed and organized into convective lines. Both observations and simulations indicated that, during the first and second stages of the warm region rainstorm, there was not only the development of convective cells on the southwest side of the convective line to maintain the rain band, but also the development of convective cells on the north side of the convective line along the direction perpendicular to the convection line. These convective cells on both sides were triggered by the cold outflow from the convective line. Notably, the cold outflow appeared not only along the convective line direction, but also along the direction perpendicular to the convective line. The latter was able to enhance and expedite the formation of a larger-scale MCS.

The different styles of echo-trainings analyzed above appear to be similar to that of the extreme rainfall events over the western coastal region of Guangdong by Wang et al. (2014) and in east China by Yali Luo et al. (2014), but differ in the duration of the third stage of echo-trainings. In the study of Wang and Yali Luo, the eastward ‘‘band training’’ of the several parallel rainbands along the quasi-linear MCS (as the third stage of echo-trainings) was the main organization form of convection, and the duration of repeated convective back building and subsequent northeastward “echo training” of multiple convective cells along the individual rainband (as the first and second stages of echo-trainings) was relatively short, which is the opposite to what we got above (Luo et al., 2014; Wang et al., 2014). What’s more, our results also showed a possible linkage between the gravity wave and the initiation of first stage echo-trainings, which could provide a new idea for research of the rainstorm over South China warm region. However, the generation mechanism of the low-level gravity wave and its relationship with the warm advection and topography are still unclear. So in a forthcoming study, we will analyze the relationship between the gravity wave and topography and low-layer warm advection by designing some sensitivity experiments.

Acknowledgements This study was jointly supported by State Key Laboratory of Severe Weather, Chinese Academy of Meteorological Sciences (2015LASW-A07), the National Natural Science Foundation of China (Grant No. 41530427) and the National Basic Research Program of China (2013CB430103).

References

Aylward R P, Dyer J L (2010). Synoptic environments associated with the training of convective cells. Weather Forecast, 25(2): 446–464

Bauer-Messmer B, Smith J A, Baeck M L, Zhao W (1998). Heavy rainfall: contrasting two concurrent Great Plains thunderstorms. Weather Forecast, 12(4): 785–798

Chen M, Wang Y, Xiao X, Gao F (2013). Initiation and propagation mechanism for the Beijing Extreme heavy rainstorm clusters on 12 July 2012. Acta Meteorol Sin, 71(4): 569–592 (in Chinese)

Gong D L, Wu Z M, Gang F (2005). Analysis of the mesoscale characteristics about a severe thunderstorm in North China. Chin J Atmos Sci, 29(3): 453–464 (in Chinese)

Hitchens N M, Brooks H E (2013). Preliminary investigation of the contribution of supercell thunderstorms to the climatology of heavy and extreme precipitation in the United States. Atmos Res, 123: 206–210

Huang X, Chen J, Ye C (2010). Doppler radar echo characteristic analysis of an extraordinary rainstorm caused by BILIS in southeastern Hunan Province. Transactions of Atmospheric Sciences, (01): 7–13

Kawashima M (2016). The role of vertically propagating gravity waves forced by melting-induced cooling in the formation and evolution of wide cold-frontal rainbands. J Atmos Sci, 73(7): 2803–2836

Ke W, Yu X, Lin W, Huang E, Guan X, Huang T, Yang X (2012). Analytical study of a torrential rainstorm caused by “echo-training”. Meteorol Monogr, 38(5): 552–560 (in Chinese)

Knupp K R, Cotton W R (1987). Internal structure of a small mesoscale convective system. Mon Weather Rev, 115(3): 629–645

Koch S, Jamison B, Lu C, Smith T, Tollerud E, Girz C, Wang N, Lane T, Shapiro M, Parrish D, Cooper O (2005). Turbulence and gravity waves within an upper-level front. J Atmos Sci, 62(11): 3885–3908

Koch S, O’Handley C (1997). Operational forecasting and detection of

mesoscale gravity waves. Weather Forecast, 12(2): 253–281

Kuester M, Alexander M, Ray E (2008). A model study of gravity waves over hurricane Humberto (2001). J Atmos Sci, 65(10): 3231–3246

Lane T, Moncrieff M (2008). Stratospheric gravity waves generated by multiscale tropical convection. J Atmos Sci, 65(8): 2598–2614

Li H J, Li X, Fang H, Li J, Qin C (2013). Analyses on triggered MCC evolution process and structural characteristic in a heavy rainstorm in Guangxi. Plateau Meteorol, 32(3): 806–817 (in Chinese)

Li M (1978). The triggering effect of gravity wave on the heavy rainstorm. Chin J Atmos Sci, 2(3): 201–209 (in Chinese)

Luo Y, Gong Y, Zhang D L (2014). Initiation and organizational modes of an extreme-rain-producing mesoscale convective system along a Mei-Yu Front in East China. Mon Weather Rev, 142(1): 203–221

Maddox R A, Chappell C F, Hoxit L R (1979). Synoptic and mesoscale aspects of flash flood event. Bull Amer Meteor Soc, 60

Nachamkin J E, Cotton W R (2000). Interactions between a developing mesoscale convective system and its environment. Part II: numerical simulation. Mon Weather Rev, 128(5): 1225–1244

Nachamkin J E, McAnelly R L, Cotton W R (2000). Interactions between a developing mesoscale convective system and its environment. Part I: observational analysis. Mon Weather Rev, 128 (5): 1205–1224

Nelson S P (1987). The hybrid multicellular–supercellular storm—An efficient hail producer. Part II: general characteristics and implications for hail growth. J Atmos Sci, 44(15): 2060–2073

Nelson S P, Knight N C (1987). The hybrid multicellular–supercellular storm—An efficient hail producer. Part I: an archetypal example. J Atmos Sci, 44(15): 2042–2059

Qi L, Nong M, Ji W (2012). Meso-scale characteristics of a rainstorm process in Guangxi Province between July, 2 and July, 4, 2009. Meteorol Monogr, 38(4): 438–447 (in Chinese)

Shou S, Li S, Yao X (2003). Mesometeorology. Beijing: Meteorological Press (in Chinese)

Skamarock W C, Klemp J B, Dudhia J (2008). A description of the Advanced Research WRF version 3. NCAR Tech. Note TN-4751STR, 113

Sun J, He N, Guo R, Chen M (2013). The configuration change and train effect mechanism of multi-cell storms. Chin J Atmos Sci, 37(1): 137–148 (in Chinese)

Sun J, He N, Wang G, Chen M, Miao X, Wang H (2012). Preliminary analysis on synoptic configuration evolvement and mechanism of a torrential rain occurring in Beijing on 21 July 2012. Torrential Rain and Disasters, 31(3): 218–225

Sun S, Zheng J, Zhi S, Xu A, Chen Y, Sheng Z, Yu A (2015). Study on a Meiyu front rainstorm caused by “echo-training”. Plateau Meteorol, 34(1): 190–201

Wang H, Luo Y, Jou B J D (2014). Initiation, maintenance, and properties of convection in an extraordinary rainfall event during SCMREX: observational analysis. J Geophys Res Atmos, 119(23): 13,206–13, 232

Weisman M L, Klemp J B (1984). The structure and classification of numerically simulated convective storms in directionally varying wind shears. Mon Weather Rev, 112(12): 2479–2498

Xia D, Zheng L, Dong S, Song L (1983). Several mesoscale separation operators for meteorological field and their comparison. Chin J Atmos Sci, 7(3): 303–311 (in Chinese)

Xue J (2000). Study on the Heavy Rainfall of Summer in 1994 in Southern China. Beijing: Meteorological Press, 1–370 (in Chinese)

Xu Y, Yan J, Wang Q, Dong J (2013). A low layer gravity wave triggering mechanism of heavy rain in the warm region of Southern China. Plateau Meteorol, 32(4): 1050–1061 (in Chinese)

Yin J, Wang D, Zhai G (2014). A study of characteristics of the cloud microphysical parameterization schemes in mesoscale models and its applicability to China. Advances in Earth Science, 29(2): 238–249

Zhao Y, Wang Y (2009). A review of studies on torrential rain during pre-summer flood season in South China since the 1980’s. Torrential Rain and Disasters, 28(03): 3–38

Zülicke C, Peters D (2006). Simulation of inertia–gravity waves in a poleward-breaking Rossby Wave. J Atmos Sci, 63(12): 3253–3276